Tetraperoxotitanates for High Capacity Direct Air Capture of Carbon Dioxide

Karlie Bach, Eduard Ribó Garrido, Jacob S. Hirschi, Zhiwei Mao, Lev N. Zakharov, Tim J. Zuehlsdorff, May Nyman*

Department of Chemistry, Oregon State University; Corvallis, OR 97331 USA

*correspondence: may.nyman@oregonstate.edu

Abstract

Materials chemists play a strategic role towards meeting ambitious global climate goals of net-zero CO_2 emissions by 2050. It is important to develop a suite of direct air capture (DAC) materials that can effectively remove legacy CO_2, bringing the atmospheric concentration closer to pre-industrial levels, and halt the current steady rise. A diversity of DAC materials will improve flexible functionality in varying ambient conditions, and bring forth a better understanding of CO_2 chemisorption and physisorption mechanisms. In our current contribution to this mission, we have developed a general synthesis for $A_4Ti(O_2)_4$ (A=Li, Na, K), alkali tetraperoxotitanates, and present their crystal structures and DAC reactivity in both ambient year-long experiments and enriched CO_2 environment studies. Characterization of DAC products by CHN analysis, thermogravimetry-mass spectrometry (TGA MS), Fourier transform infrared spectrometry (FTIR), Raman spectrometry, powder X-ray diffraction (PXRD), and scanning electron microscopy-energy dispersive X-ray spectrometry (SEM EDX) all point toward a mechanism of Ti-centered CO_2 chemisorption for the K-analogue, and hydrolysis/autodegradation for the Li and Na analogues. $K_4Ti(O_2)_4$ exhibits remarkable DAC capacity of 8.73 mmol CO_2/gram sorbent, reaching nearly maximum capacity in 20 days. This translates to nearly three CO_2 molecules chemisorbed, per Ti-center. $Na_4Ti(O_2)_4$ and $Li_4Ti(O_2)_4$ are much slower, but also with high capacity (respectively 6.74 and 8.33 mmol CO_2/gram sorbent). Characterization of the $Na_4Ti(O_2)_4$ DAC products via SEM EDX elemental mapping and imaging shows phase separation of Na-rich and Ti-rich phases in a core-shell morphology, where the Ti-rich core is largely passivated by the Na-rich coating. This both sheds light on its poorer and delayed performance, and also points toward the superior performance of Ti^{IV} in CO_2 chemisorption by DAC, in comparison to its alkali counter cations.

Introduction

Since the advent of the industrial revolution and the increasing reliance on fossil fuels, levels of atmospheric CO_2 have risen from an average of 278 ppm (pre-industrial) to nearly 430 ppm (current), influencing extreme climate events that lead to loss of ecosystems, property and lives, in addition to chronic disease and extinction of populations. Although moving towards lower carbon or carbon neutral sources of energy is necessary to halt the rising rates, technologies are also needed to bring atmospheric CO_2 back to more benign levels. Technologies, materials and processes for carbon dioxide removal (CDR) are being innovated for both direct air capture (DAC) and point source capture.[1-3] A major challenge for DAC materials is high selectivity in dilute conditions, while the unique challenge for point-source capture is stability at harsh operating conditions, and selectivity over other gases in the industrial exhaust. Common synthetic CDR materials (both point-source and DAC) include alkali and alkaline earth hydroxides,[4-7] clays and other minerals,[8,9] layered double hydroxides, [10-12] zeolites,[13] solid and liquid amines,[14,15] ionic liquids,[16] and MOFs.[17] The vast majority of these technologies and materials function as chemisorbants, meaning the CO_2 is converted to carbonate or carbamate as the capture and sequestration product.

Some of the challenges with the alkali and alkaline earth hydroxide solids and solutions for CO_2 chemisorption is passivation (solids), high corrosivity (solutions) and high regeneration temperatures (solids and solutions). The same stabilization energy that favors carbonate formation also disfavors its decomposition to release the captured CO_2, as one common means of sorbent regeneration. For example, decomposition temperature is >900 °C for $CaCO_3$.[18] High oxidation state transition metals (including Mo^{VI}, Ti^{IV}, Zr^{IV}, W^{VI}, V^{V}), usually in the form of oxides or dissolved oxoanions, have served various supporting roles in CDR technologies including lowering regeneration temperature, catalyzing CO_2 hydration for chemisorption, and in some cases chemical reduction for CO_2 'fixing'.[19-27]

Reactive oxygen species, i.e. superoxide (O_2^-) is one of the oldest DAC materials; potassium superoxide has been used as an air scrubber for space travel, because it both captures CO_2 and releases oxygen. However, studies have shown that the mechanism of DAC is via decomposition of KO_2 to KOH in the presence of atmospheric water, which then performs the DAC. With rigorous exclusion of water, the CO_2 capture reaction does not proceed beyond the trace amount of hydroxide present in the KO_2.[28] Kravchuck[29] synthesized potassium uranyl diperoxide monosuperoxide and demonstrated its DAC behavior, yielding $K_4UO_2(CO_3)_3$ over 2-3 months. We recently showed formation of $Cs_4UO_2(CO_3)_3$ within a few hours from uranyl triperoxide,[30] where the high reactivity is attributed to the Cs-cation, but the role of the alkali countercation is poorly understood. These uranyl molecules, although controversial in their use for DAC given the mild radioactivity of depleted uranium,[30] exhibit rapid and moderately high capture capacity metrics, respectively 5.74 (K) and 3.34 (Cs) mmol CO_2/g sorbent.

Given the promising DAC performance of the uranyl peroxides, the Periodic Table relationship between uranyl and the early d^0 transition metals (TM, namely Mo^{VI}, W^{VI}, V^V, Nb^V, Ta^V), and reported synthesis of their tetraperoxometalate species,[31-41] we have been investigating the DAC behavior of this family of compounds. We demonstrated via a year-long DAC study the mechanism of $V(O_2)_4^{3-}$ (tetraperoxovanadate) carbon capture directly involves the vanadium-center, and the first DAC product that forms is $VO(O_2)(CO_3)^{3-}$.[42] Over the course of the year-long study, the alkali $V(O_2)_4^{3-}$ DAC products (alkali (A) = K, Rb and Cs) degraded to AVO_3 plus $AHCO_3$ and A_2CO_3. The first observed DAC product, ($VO(O_2)(CO_3)^{3-}$), had a low CO_2 release temperature of ~350 ºC, demonstrating the importance of the high oxidation state metal in both CO_2 chemisorption and release. Although we observed more rapid DAC with the heavier alkalis (similar to the uranyl peroxide compounds), the conversion of peroxide to carbonate maxed out at around 1.5 – 2 CO_2 molecules per metal center.

Following these studies, we were interested in the DAC behavior of peroxotitanate compounds. Titanium is both 100× more abundant and 100× cheaper than vanadium. In addition, benchmarking the DAC performance of putative $Ti(O_2)_4^{4-}$ molecules would yield fundamental insight into the trends of the d^0-TM peroxide DAC behavior, based on size and charge of the TM, recently studied by computation.[43] Interestingly, the synthesis of tetraperoxotitanates was reported for the first and last time in 1928,[44] without the benefits of modern instrumentation for characterization. Thermal and photodecomposition of potassium tetraperoxotitanate was reported in the 1980s,[45,46] and the authors referred to the 1928 paper for their synthesis; which makes this the only reported synthesis of putative $Ti(O_2)_4^{4-}$. There have been a few reports of heteroleptic titanium peroxide complexes;[47-49] again, with almost no crystal structures. Yet titanium peroxide molecules and materials have noted applications in catalysis,[50-52] materials synthesis,[53-56] and nuclear waste treatment.[57] Moreover, Ti-peroxide bonding with its characteristic orange color is universally exploited for detection of formed peroxides in organic reagents.[58] Therefore, in addition to investigating the DAC behavior of tetraperoxotitanate compounds, we saw this as an opportunity to develop the synthesis and atomic level-description of materials whose transient states have been detected and exploited.

Here we report the synthesis, crystal structures, and DAC capacity, rates and mechanisms of Li, Na and K salts of $Ti(O_2)_4^{4-}$ (**TPTi**, tetraperoxotitanate) anions. Similar to the uranyl and vanadium peroxide materials, the titanium peroxides exhibit an alkali-dependent capture capacity and reactivity rate, but with a trend break: K>Li>Na. Not only is K-**TPTi** the most effective DAC material with a capacity of 8.73 mmol CO_2/g sorbent, it also exhibits a different reaction mechanism than Na-**TPTi** and Li-**TPTi,** based on characterization of the DAC/ambient-aged products, and those exposed to an CO_2-enriched environment. Specifically, K-**TPTi** shows evidence for direct Ti-carbonate bonding following rapid DAC, while Li-**TPTi** and Na-**TPTi** undergo autodegradation and phase separation, followed by delayed DAC of the alkali-rich

phases. In absence of a crystal structure evidencing direct Ti-carbonate binding as a chemisorption mechanism, we used computation to help explain spectroscopic signals that point towards the presence of Ti-carbonate bonding for K-**TPTi**, but not necessarily Na-**TPTi** and Li-**TPTi**.

Results and Discussion

Synthesis. Synthesis and crystallization (details in the SI) of the tetraperoxotitanates were generally carried out by heating an AOH solution with TiO_2 and H_2O_2 until all solids dissolved and a clear, pale yellow solution was obtained. After cooling, isopropanol was added directly to the solution in the case of sodium and potassium, and via solvent diffusion in the case of lithium, to promote crystallization. Different concentrations of hydroxide, plus TiO_2 per volume reaction solution are summarized in **Table S1**. The initial procedure was developed following the prior-reported synthesis in which $Na_4Ti(O_2)_4$ was believed to be a potential intermediate in the synthesis of peroxide-decorated titanate materials for nuclear waste treatment.[57] In this prior study, molecular titanium alkoxide or $TiCl_4$ (aq HCl) was used as the titanium source. Because these forms of titanium are unstable in storage, have reaction byproducts that are reactive with peroxide and sometimes promote poor reproducibility, we adapted the synthesis to use benign, inexpensive, and air-stable TiO_2. The disadvantage, however, is poorer solubility in the reaction media. Synthetic conditions were then modified for Li and K, largely based on the alkali solubility, and the TiO_2 solubility in the alkali hydroxide/peroxide mixture. We also attempted to prepare a Cs-TPTi, but this solution never crystallized, indicating high solubility of this analogue. The yields of all three synthesized compounds are very high, over 90%. They generally grow as colorless crystals, and only turn yellow upon ambient exposure during the DAC studies. The yellow color is indicative of partial protonation or H-bonding association of the peroxide ligands with water, and/or formation of Ti-carbonate complexes or peroxycarbonate complexes.

Structure descriptions. We are describing for the first time the crystallographic structures of any $A_4Ti(O_2)_4$ compounds, the crystallographic data are summarized in **Table S2**. Single crystal X-ray diffraction (SCXRD) revealed the following formulas: $K_4Ti(O_2)_4{\cdot}10H_2O$ (**K-TPTi**), $Na_4Ti(O_2)_4{\cdot}3H_2O$ (**Na-TPTi**), and $Li_4Ti(O_2)_4{\cdot}10.5H_2O$ (**Li-TPTi**). Key bonding metrics are summarized in **Table 1** and discussed below. All three compounds feature the $[Ti(O_2)_4]^{4-}$ anion, with four O_2^{2-} peroxide ligands in a roughly tetrahedral arrangement around the Ti^{IV} center (**Figure 1F**). The O_p-O_p peroxide bond length and Ti-O_p bond length are very consistent between each alkali analogue, with average O_p-O_p bond lengths of 1.5 Å and average Ti-O_p bond lengths of 2.0 Å in all three structures. Average bond distances with appropriate significant figures and errors are summarized in **Table 1**. The biggest difference between the three tetraperoxotitanate anions is the O_p-Ti-O_p interperoxide bond angles (highlighted in **figure 1F**), exhibiting different degrees of distortion, likely due to differential interactions with the alkalis and water in the crystal lattice. The angles were measured to the center of the O_p-O_p bonds to best illustrate the tetrahedral structure (black dashed lines in **Figure 1F**). The Li-analogue exhibits four O_p-Ti-O_p angles at 99.2°, and two at 133.0°. The Na-analogue has four O_p-Ti-O_p angles at 99.7° and two at 131.5°. The K-analogue has four O_p-Ti-O_p angles at 100.3° and two at 130.0°. This trend shows that with increasing size of alkali counterion, the titanium tetraperoxide anion becomes slightly more symmetric.

The K-analogue (**Figure 1A**) crystalizes in the monoclinic space group *C*12/*c*1 with a volume of 1715.1(3) $Å^3$. The Ti-O_p bond lengths range between 1.963(5) – 2.041(28) Å, and O_p-O_p (intraperoxide) distances are 1.485(5) – 1.499(6) Å. Each tetraperoxotitanate anion is directly associated with four

potassium cations with O_p-K bond lengths ranging from 2.689(5) – 3.468(3) Å, and each K^+ bridges two peroxotitanate anions. Water within the crystal lattice bonds to the potassium with K-O bond lengths ranging from 2.669 (6) – 3.116(6) Å. The water molecules hydrogen-bond to the peroxide ligands with O_{water}----O_p distances ~2.75 Å.

The Na-analogue (**Figure 1B**) crystalizes in the monoclinic space group $P12_1/c1$ with a unit cell volume of 900.66(5) $Å^3$. The smaller unit cell volume is attributed to significantly less water in the crystal lattice, in comparison to the other two analogues. The Ti-O_p bond lengths range between 1.9609(9) – 2.024(1) Å, and intraperoxide O_p-O_p distances are 1.505(1) – 1.513(1) Å. Each tetraperoxotitanate anion is directly surrounded by 11 sodium cations with O_p-Na bond lengths ranging from 2.308(1) – 2.906(1) Å. Water within the crystal lattice bonds to the sodium with Na-O bond distances ranging from 2.325(1) – 2.927(1) Å. The water molecules hydrogen-bond to the peroxide ligands with O_{water}----O_p distances ~2.82 Å.

The Li-analogue (**Figure 1C** and **1D**) crystalizes in the space group $P2n1$ with a cell volume of 1438.7(2) $Å^3$. The unit cell contains two unique $[Ti(O_2)_4]^{4-}$ anions that are aligned along the *b*-axis in a staggered fashion. The observed alignment is similar to a 2_1 screw axis, but the 180° rotation and translation along the *b*-axis replicates the Ti1 complex to the Ti2 complex. The actual symmetry element is a simple translation. The Ti-O_p bond lengths range between 1.958(6) – 2.017(8) Å for one unit and 1.960(8) – 2.037(7) Å for the second. The O_p-O_p intraperoxide distances within each anion are 1.51(1) – 1.521(9) Å, and 1.48(1) – 1.503(9) Å respectively. Different from the Li and Na analogues, the tetraperoxotitanate anions are not directly bonded to any lithium, so there are no O_p-Li bonds present. Instead, the $[Ti(O_2)_4]^{4-}$ units sit between layers of rings of 10 lithium bridged by water molecules (**Figure 1E**). The Li-O_{water} bonds lengths range from 1.90(2) – 2.28(2) Å; and the Li are tetrahedrally or octahedrally bonded. The formation of Li-water rings and cages has been observed prior in lattices with polyatomic anions; i.e. with the $[Nb_6O_{19}]^{8-}$ polyoxometalate.[59,60] The water molecules hydrogen-bond to the peroxide ligands with O_{water}----O_p distances ~2.73 Å, holding the layers together.

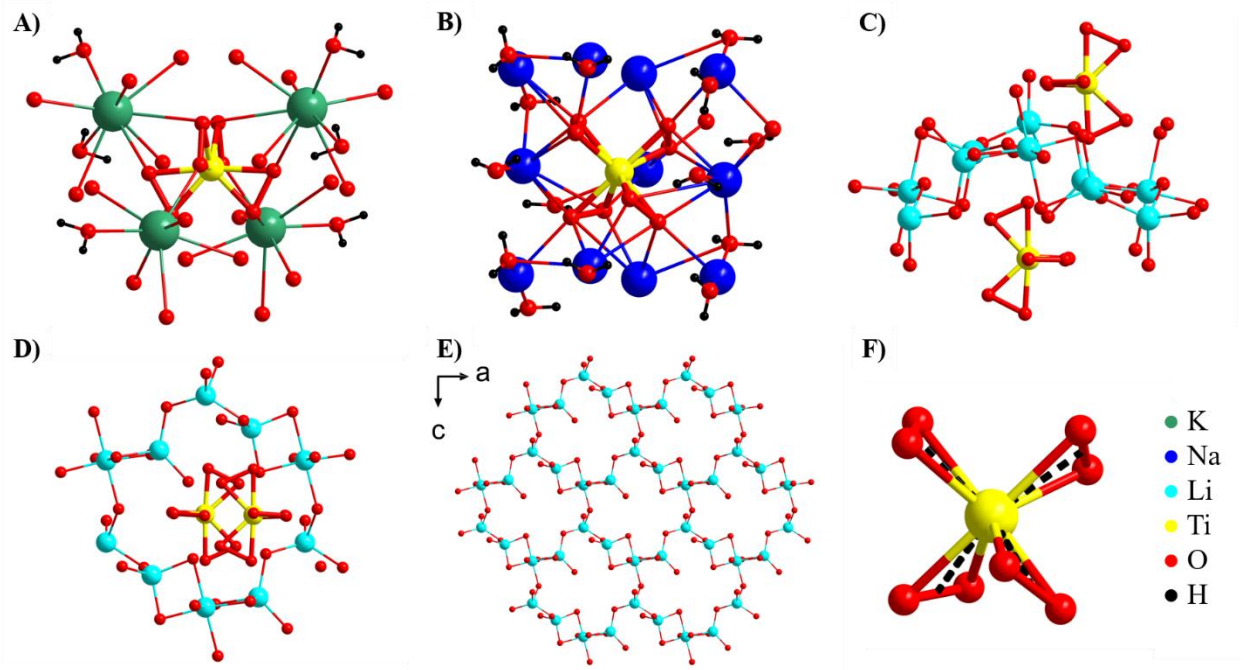

Figure 1. Representative ball-and-stick views of alkali tetraperoxotitanates. (A) **K-TPTi** viewed along the *c*-direction, highlighting the K^+-peroxotitanate bonding. All oxygens bonded to K^+ and pointing away from the TPTi unit are water molecules. (B) **Na-TPTi** viewed along the *a*-direction, highlighting Na^+-peroxotitanate bonding. (C-E) **Li-TPTi** viewed along the *c*-direction (C), and *b*-direction (D), highlighting the lack of direct bonding between lithium and the peroxotitanate anions. (E) Li-water ring layer viewed on the *ac* plane, and (F) tetraperoxotitanate common anion observed for all analogues. Dashed black lines were used to measure the pseudo-tetrahedral O_p-Ti-O_p angles summarized in **Table 1**. No hydrogen atoms of water molecules were directly located in the electron density map; rather they were modeled (**see SI**).

Table 1. Summary of $A_4Ti(O_2)_4$ bonding averages (Å).

Alkali cation	Ti-O_p	O_p-O_p	A^+-O_p	# A^+ bonded to each $[Ti(O_2)_4]^{4-}$	O_p-Ti-O_p bond angles
K	2.0023	1.4920	3.0576	4	100.28 (4 total) 130.03 (2 total)
Na	2.0009	1.5084	2.4881	11	99.714 (4 total) 131.49 (2 total)
Li	1.9949	1.5034	-	0	99.162 (4 total) 132.96 (2 total)

Bulk characterization. Because the tetraperoxotitanates appear so reactive to both carbon capture and hydrolysis/autodegradation (based on color change and/or evolution of bubbles), we deemed it important to characterize the bulk materials thoroughly to benchmark spectroscopic signals that evolve with air exposure. This included Powder X-Ray Diffraction (PXRD), thermogravimetry mass spectrometry (TGA-MS), and infrared spectroscopy (FTIR), supported by computational modeling and spectra simulation. These are discussed below.

PXRD (**figure 2c**) of Li-**TPTi**, unlike Na-**TPTi** and K-**TPTi** shows a good match (peak positions and most relative peak intensities) with the powder diffraction pattern calculated from the single-crystal data, indicating the single-crystal data is representative of the bulk material. The crystals have an octahedral shape (**figure 2c**, inset), which does not lead to any preferred orientation, unlike the acicular shape of the Na-TPTi and K-TPTi crystals. We also attribute the mismatch of the K-**TPTi** experimental PXRD and that simulated from the single-crystal data is its high reactivity in air (both DAC and autodegradation) leading to decomposition during data collection. As illustrated by the microscope images of the crystals under oil (**figure 2a** insert), oxygen bubbles are evolving from the K-**TPTi** crystals. Finally, while the peroxides in Li-**TPTi** are solely bound to titanium, peroxides in K and Na-**TPTi** are shared between titanium and the respective alkali. This could polarize the already reactive peroxide ligand, leading to solid-state rearrangement and/or partial degradation.

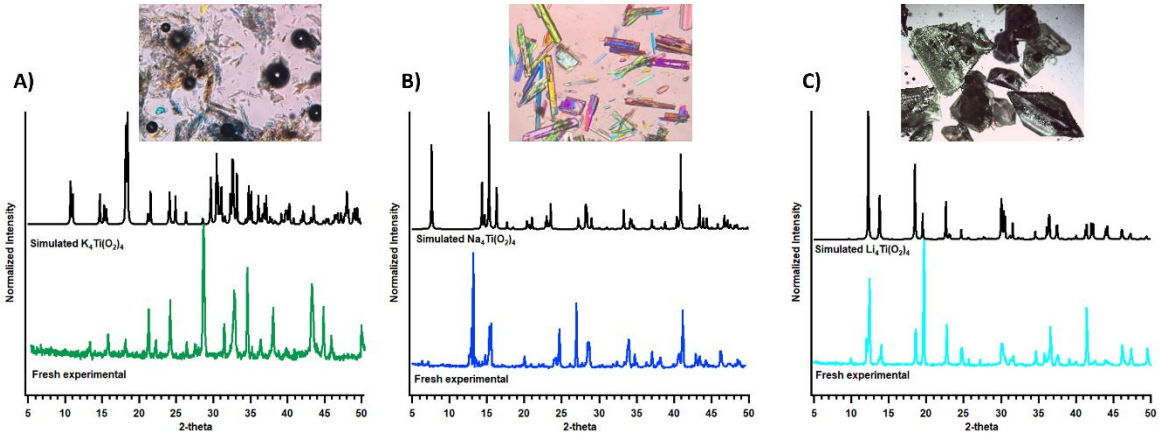

Figure 2. Simulated PXRD patterns (black) of K (green), Na (blue), and Li (turquoise) -**TPTi**. Photos above each show the respective crystals in oil under the microscope.

Thermal Gravimetric Analysis-Mass Spectrometry (TGA-MS) was used to further characterize the amount of water within the structure as secondary evidence that single-crystal is representative of bulk. The weight loss percent shown in the TGA correlates to the loss of water (from the lattice) and oxygen (from peroxide) observed in the MS signals, and was used to calculate the water in the formulae for all three structures (**Figure**). For K-**TPTi**, the water and oxygen evolve simultaneously, whereas distinct, separate steps can be observed in the weight loss curves for the Na and Li analogues. TGA-MS showed a weight loss of 45.2%, 12.5% of which can be attributed to oxygen decomposition of peroxide. The remaining 32.7% is water, in agreement with nine water molecules in the structure, which shows 10 water molecules per formula unit. Na-**TPTi** and Li-**TPTi** weight loss quantification was more straightforward, with the TGA-MS showing distinct weight loss of water at a separate temperature than the oxygen loss, with 16.0% and 45% weight loss from water respectively. This indicates three water molecules in Na-**TPTi** and 9.5 in Li-**TPTi**, again matching well with single crystal formulae, possessing 3 and 10.5 water molecules, respectively.

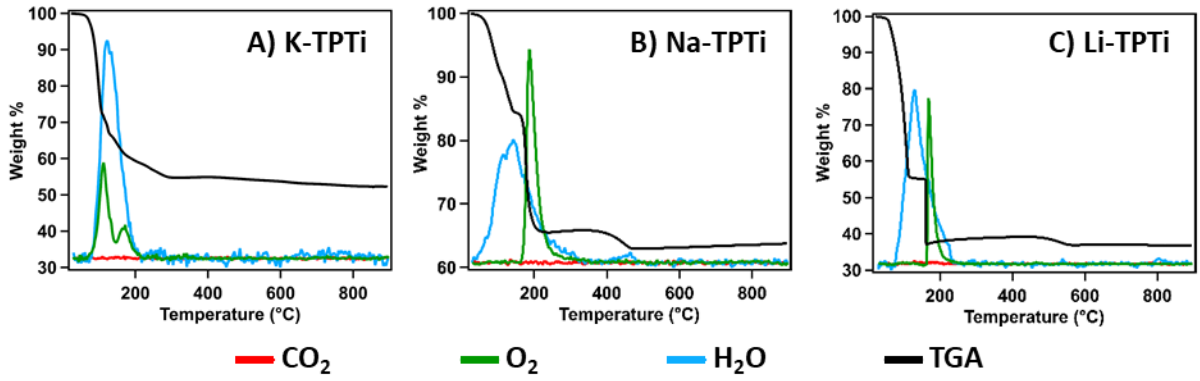

Figure 3. TGA-MS of fresh peroxotitanates. The percentage weight loss shown from the TGA curve (black) that aligns with loss of water (blue) and oxygen (green) from the MS signals agree with the formulas from SCXRD.

Figure 4 shows FTIR of all three A-**TPTi** in the Ti-O vibrational region (below 1000 cm^{-1}), with the water background removed. Spectra up to 1800 cm^{-1} are shown later (**figure 7**), for discussion of DAC behavior. We also calculated the vibrational modes for Na-**TPTi**, as an example, to interpret expected vibrations of the peroxoanion unit (**figure S1.1**). The peroxide stretching is predicted at around 820 cm^{-1} and peroxide-Ti bending motions register around 500 cm^{-1}. These are the major peaks observed in all three analogues (**figure 4**). Additional peaks are not readily explained by computation, or by comparison to other reported transition metal peroxides.[61] These additional peaks do not necessarily grow with the DAC studies, and in some cases they diminish, especially for Li-**TPTi**. We attribute these additional peaks to alkali-water bonding present in the crystalline lattice. The Li-analogue with the most structured water-alkali network has the more additional vibrations that the Na and K analogues.

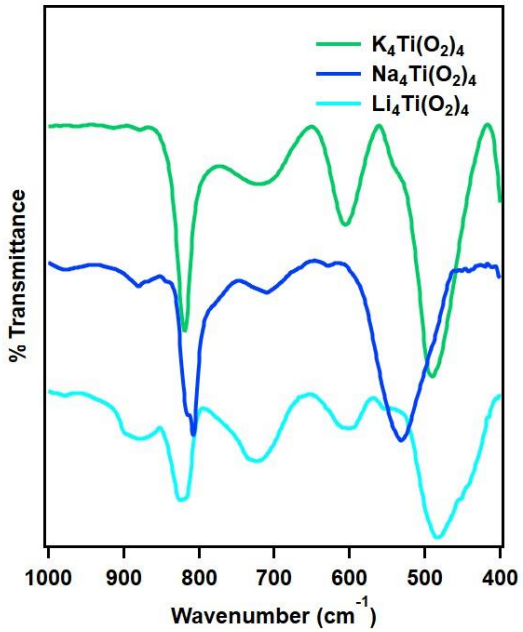

Figure 4. FTIR spectra of the three studied A-**TPTi** prior to DAC studies.

Direct Air Capture (DAC) and Enriched CO_2 Environment Studies of A-TPTi

Experiments with CO_2 capture were done in both ambient air, with samples simply placed on a lab bench (T ~ 21-23 ºC; relatively humidity ~ 30 – 50%) spread out in glass petri dishes (**figure S2**). Since these are year-long, true DAC experiments (in a lab housed in a 1939 vintage building), we experience seasonal temperature and humidity swings. Therefore, we also performed 1-3 day experiments in enriched CO_2 atmosphere, in which samples were placed into an enclosed chamber (desiccator) set above dry ice (details in SI, **figure S3**). We present data from these enriched CO_2 atmosphere products throughout, alongside various time stamps of the 1-year ambient experiments. In each case, there is a good agreement in spectroscopic analyses between the year-long DAC experiments and the enriched CO_2 chamber experiments, ensuring the swings in ambient conditions do not ultimately affect the reaction end-product. In addition, spectra across the year-long study showed consistent trends and supported the reported mechanisms that differ between K-**TPTi** and Li/Na-**TPTi**. All A-**TPTi** samples quickly turned from white to yellow within a day in the enriched CO_2 environment, and gradually evolved to yellow in ambient air (**figure S2**). The yellow color can certainly be attributed to protonated peroxide ligands, and may also be attributed to a Ti-carbonate complex, similar to the prior-reported vanadium peroxide carbonate complex.[42] The color change rate orders K-**TPTi** > Li-**TPTi** > Na-**TPTi**, commensurate with DAC rates, monitored by CHN microanalysis, TGA-MS, FT-IR, and PXRD.

Prior to describing the spectroscopic evidence of different reaction pathways of A-**TPTi**, we explain here the two observed pathways and define terminology used to discuss these reactions. For Li-**TPTi** and Na-**TPTi**, we observe a predominant path of hydrolysis/autodegradation, followed by DAC of the alkali-rich phase. Equations 1 and 2 simplify and summarize these reactions as (A=alkali):

$$A_4Ti(O_2)_4 + 2H_2O \rightarrow 4AOH + 2O_2 + TiO_2 \quad (1)$$

$$2AOH + CO_2 \rightarrow A_2CO_3 + H_2O \quad (2a)$$

or

$$AOH + CO_2 \rightarrow AHCO_3 \quad (2b)$$

We will refer to these reactions later as hydrolysis/autodegradation, with the following qualifiers and unknowns: 1) There is an angstrom-nanometer level mixing of the formed phases that cannot be achieved with physical mixtures of the separate oxides/hydroxides; 2) The degradation products are likely hydrous (i.e. hydrous titania). 3) There may be intermediate A-Ti oxide phases that we have not been able to isolate and identify (discussed later).

Equation 3 describes Ti-centered DAC, using the V-centered DAC product as a model compound:

$$A_4Ti(O_2)_4 + CO_2 \rightarrow A_4TiO(CO_3)(O_2)_2 + O_2 \quad (3)$$

with the caveat that although we have some spectroscopic evidence that titanium carbonate phases form, we do not have the absolute evidence of a crystal structure, and we do not know what species are present. This reaction will be referred to in the discussion as Ti-centered DAC. Ti-carbonate crystal structures are scarce in the literature, and seem to require organic media and additional bulky ligands for crystallization. Reported structures include: 1) two Ti-monomers with heteroleptic, monodentate carbonate and additional bulky ligands bound to titanium;[20,62] 2) two Ti-dimers featuring C_p*Ti(III)-carbonate (C_p*=cyclopentadienyl) with both chelating and bridging carbonate.[63] On the other hand, it does not seem

unreasonable that Ti-carbonate could be a stable or metastable moiety from aqueous systems, given its periodic relationship with vanadium to the right, and diagonal niobium.

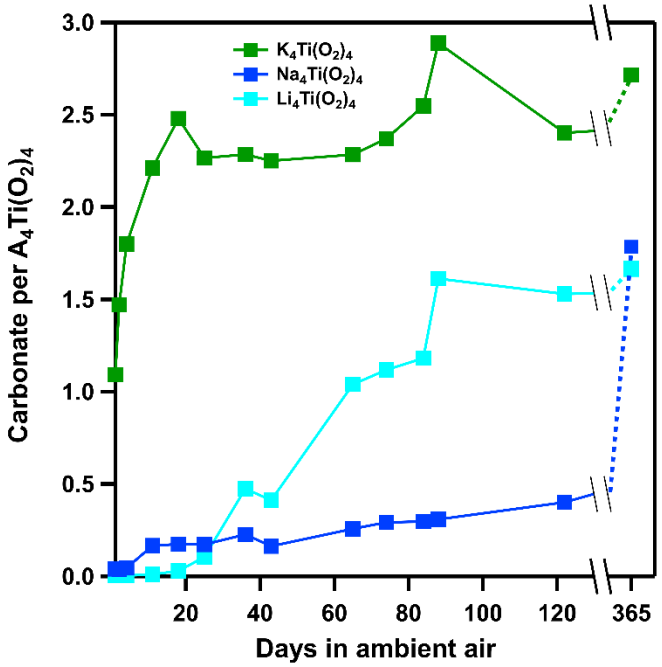

Figure 5. Carbon capture capacity of K-**TPTi**, Na-**TPTi** and Li-**TPTi** as determined by CHN analysis, expressed as number of CO2 captured/chemisorbed (carbonate) per titanium.

Weight percent carbon (as carbonate/bicarbonate species) determined from CHN analysis from DAC studies and enriched CO_2 environment studies, plus DAC capacity (mmol CO_2/g sorbent) of the three A-**TPTi** is compiled in **Table 2**. **Figure 5** shows carbonate/Ti in DAC studies of the three materials, also from CHN data. Measurements were initially taken every 5 days up to 25 days, every five to 20 days up to 90 days, then again at 120 days, and one year. Both Li-**TPTi** and K-**TPTi** show a decrease in captured carbon after the 90 day measurement that also increases again, indicating some equilibrium after the material reaches maximum capacity. K-**TPTi** clearly exhibits much more rapid reaction with CO_2, reaching 2.5 CO_3^{2-}/Ti at 20 days, and a maximum of 2.9 CO_3^{2-}/Ti; a theoretical 75% efficiency if we consider the peroxide to be the reactive, basic oxygen in the chemisorption reaction. Both Li- **TPTi** and Na- **TPTi** exhibit maximum chemisorption of ~1.8 CO_3^{2-}/Ti, with Li- **TPTi** clearly exhibiting a higher initial reaction rate. Na- **TPTi** only shows substantial reactivity between 120 days and 1 year. As additional characterization data reveals below, K- **TPTi** predominantly undergoes Ti-centered DAC, while Li-TPTi and Na-TPTi undergo hydrolysis/autodegradation DAC, where the alkali-rich phase (i.e. alkali hydroxide) is the reactive DAC material, and the observed delay in DAC is related to the initial autodegradation process that activates the material. All three materials ultimately have excellent DAC capacity (**Table 2),** especially K-TPTi with both rapid kinetics and direct reaction of the peroxotitanate, and a maximum capacity of nearly 9 mmol CO_2/gram sorbent.

Table 2. Carbon capture capacity for A-TPTi (A=K, Na, Li)

A-TPTi	DAC maximum carbonate per Ti	Enriched CO_2 Environment, maximum carbonate per Ti	DAC capacity mmol CO_2/g sorbent[1]
$K_4Ti(O_2)_4$	2.9	2.6	8.73
$Na_4Ti(O_2)_4$	1.8	1.8	6.74
$Li_4Ti(O_2)_4$	1.7	1.5	8.33

[1]*estimated based on anhydrous formula since the amount of water varies depending on atmospheric condition, with time, and composition*

TGA-MS was used as a second means to quantify CO_2 uptake, and determine the temperatures at which CO_2 is released as a function of heating the different ambient DAC A-**TPTi** time study products (**figure 6**). This both provides information about how the carbonate is bound (i.e. to the alkali or the Ti^{IV}), its speciation (HCO_3^- or CO_3^{2-}), and whether hydrolysis/autodegradation outcompetes the Ti-centered DAC reaction, or vice versa. Total weight percent carbon, as determined by TGA-MS, compared to that determined by CHN analysis showed good agreement (**Table S3**). The TGA-MS of the pre-exposed A-**TPTi** was shown earlier for comparison (**figure 3**). Here we show A) A- **TPTi** aged for 3 months (~90 days), because there is large contrast in the percent CO_2 captured as determined by CHN analysis (**figure 5**) for the three alkali-analogues, B) aged for 1 year, representing the end of the experiment and also as a comparison to CO_2 captured in an enriched CO_2 environment, shown in C). Also exhibited is TGA-MS analysis of physical mixtures of alkali bicarbonate plus TiO_2 (Na and K) and alkali carbonate plus TiO_2 (Li) as standards (D).

For Na-TPTi, the least reactive compound, Ti-bound peroxide is still observed after 3 months on the lab bench, indicated by large oxygen peak at 200 ºC, which matches that of the 'fresh' Na-TPTi (**figure 3**). Minimal CO_2 is observed, only a discernable rise in the CO_2 signal at 900 °C at the end of the heating experiment, likely the initiation of decomposition of Na_2CO_3 at >900 ºC.[18] This is consistent with the CHN analysis with minimal carbon detected. On the other hand, only a small amount of peroxide remains for the Li-TPTi, and even less for K-TPTi, based on the O_2 mass spectra signals, and also consistent with the reactivity rate that is related to the alkali, uniformly shown by all reported analyses. The 1-year ambient DAC and the 3-day enriched CO_2 atmosphere Na-**TPTi** are almost identical, and also similar to the TiO_2-$NaHCO_3$ physical mixture. This indicates the Na- **TPTi**, the most stable of the three $Ti(O_2)_4^{4-}$ analogues, undergoes slow hydrolysis/autodegradation, and the Na-rich phase (i.e. NaOH) becomes the reactive DAC material. The major difference between the reacted Na- **TPTi** (**figure 6B** and **6C**) and the standard TiO_2-bicarbonate (**figure 6D**) is the former have an additional CO_2 peak at 645 °C, likely related to TiO_2-catalyzed CO_2 release, discussed in more detail below.

At 3 months aging, the Li- **TPTi** DAC product releases the majority of its captured CO_2 at 433 ºC, in addition to a growing peak above 800 ºC. The latter is attributed to Li_2CO_3, where a lithium-rich phase such as LiOH is serving as the DAC material, following the hydrolysis/autodegradation of Li- **TPTi**, also indicated by the delayed reactivity (**figure 5**). The former (433 ºC) we attribute to TiO_2-catalyzed lower-temperature decomposition of carbonate. Small, charge-dense and oxophilic Ti^{IV} readily polarizes carbonate C-O bonds, lowering carbonate thermal decomposition temperature. We observed this prior for the analogous tetraperoxovanadate DAC materials;[42] and Bhatti and co-workers also observed this catalytic effect of various early transition metal oxides (MoO_3, WO_3, V_2O_5, TiO_2, Cr_2O_3) on the regeneration of

aqueous MEA (monoethanolamine) point-source CDR solutions.[25] Interestingly, we did not observe the 433 ºC peak (or anything similar) in the TGA-MS analysis of the physical mixture of TiO_2 and Li_2CO_3, likely due to 1) the hydrous nature of the decomposed Li-TPTi, decreasing thermal activation temperature of carbonate, where proton association of the carbonate serves a similar role as the high oxidation state metals, and 2) the nanometer to angstrom level mixing of the hydrous titania and lithium carbonate in decomposed Li-TPTi that cannot be achieve by physically mixing of the separate powders. Unlike the Na and K analogues, the Li analogue shows the greatest differences between the 1-year ambient aging and 3 day CO_2 enriched atmosphere aging, perhaps related to the well-known but poorly-understood metastability of putative $LiHCO_3$.[64] While almost no water is detected in the MS profile of Li- **TPTi** exposed to an enriched CO_2 environment (**figure 6C**), the Li- **TPTi** exposed to ambient conditions for one year (**figure 6B**) has considerable water (10 wt %), released at 200 °C. Moreover, the Li- **TPTi** from the CO_2-enriched atmosphere has a small CO_2 peak below 200 °C, where we might expect putative $LiHCO_3$ to decompose, consistent with the Na and K analogues (**figure 6D**). Alternatively, this peak represents Ti-bond carbonate, since it is simultaneously released with oxygen, as observed for the $VOCO_3(O_2)_2^{3-}$, prior.[42] Nonetheless, despite the excellent DAC capacity (8.33 mmol/g sorbent) of Li- **TPTi**, the true DAC material is a poorly-characterized nanoscale mixture of hydrolysis/autodegradation products.

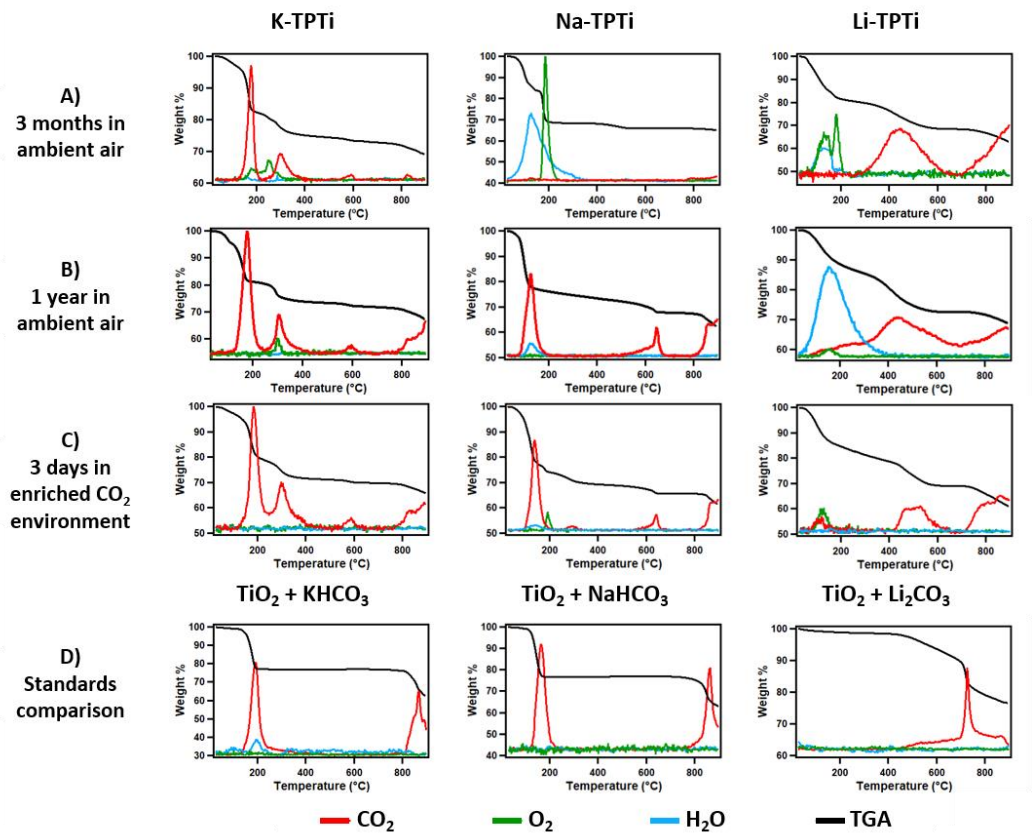

Figure 6. TGA-MS analysis of the three studied **TPTi** ambient-atmosphere and CO_2-enriched environment reaction products, plus standards.

The 3-month aged K- **TPTi** TGA-MS profile closely resembles that of the 1-year DAC sample and the 3-day CO_2 chamber sample, consistent with the rapid DAC behavior of K- **TPTi**, nearly reaching maximum capacity in 20 days (**figure 5**). The unique feature of these CO_2 TGA-MS signals is the additional peak at 300 °C, which based on comparison to $VOCO_3(O_2)_2^{3-}$,[42] we attribute to Ti^{IV}-bound carbonate. These also exhibit $KHCO_3$ decomposition at 175 °C, and K_2CO_3 decomposition, >800 °C. The analogous $VOCO_3(O_2)_2^{3-}$ [42] featured simultaneous release of metal-bound peroxide (as O_2), which is also observed for K- **TPTi**, but to a lesser extent. These results indicate that K-**TPTi** undergoes both Ti-centered DAC, and hydrolysis/autodegradation, or the intermediate and presumably metastable (based on lack of known crystal structures) Ti-carbonate species degrade to titania plus potassium bicarbonate. Nonetheless, the much faster completion of the K- **TPTi** DAC reaction (**Figure 5**) suggests this differentiated reaction pathway is important to material performance.

CO_2 Capture Analysis via FTIR. FTIR was useful in confirming DAC reaction pathways for the three A- **TPTi**, as well as attempting to identify vibration modes consistent with Ti-bound carbonate, specifically for K- **TPTi**. The simplest spectra are Li-TPTi (**figure 7C**), perhaps due to the minimal presence of bicarbonate and a clean hydrolysis/autodegradation pathway. The Ti-bound peroxide is still apparent at 57 days of DAC. By TGA-MS, Ti-bound peroxide remains at ~90 days as well (**fig. 6A**), but both methods indicate the peroxide has all reacted by 1 year. The Li_2CO_3 peaks (859, 1417, 1486 cm^{-1}) grow in gradually, evident at 28 days. The broad peak at 1548 cm^{-1} in the Li- **TPTi** from the enriched CO_2 environment may indicate bicarbonate, also possibly observed in the TGA-MS of the same material. There is an increased absorption at low wavenumber for both the Li- **TPTi** and Na- **TPTi** experiments that is not observed in the K- **TPTi** experiments. This could either be TiO_2 (**figure S4**) or water. Simply put, the FTIR agrees with the TGA-MS that hydrolysis/autodegradation is the prevalent DAC reaction for Li- **TPTi**.

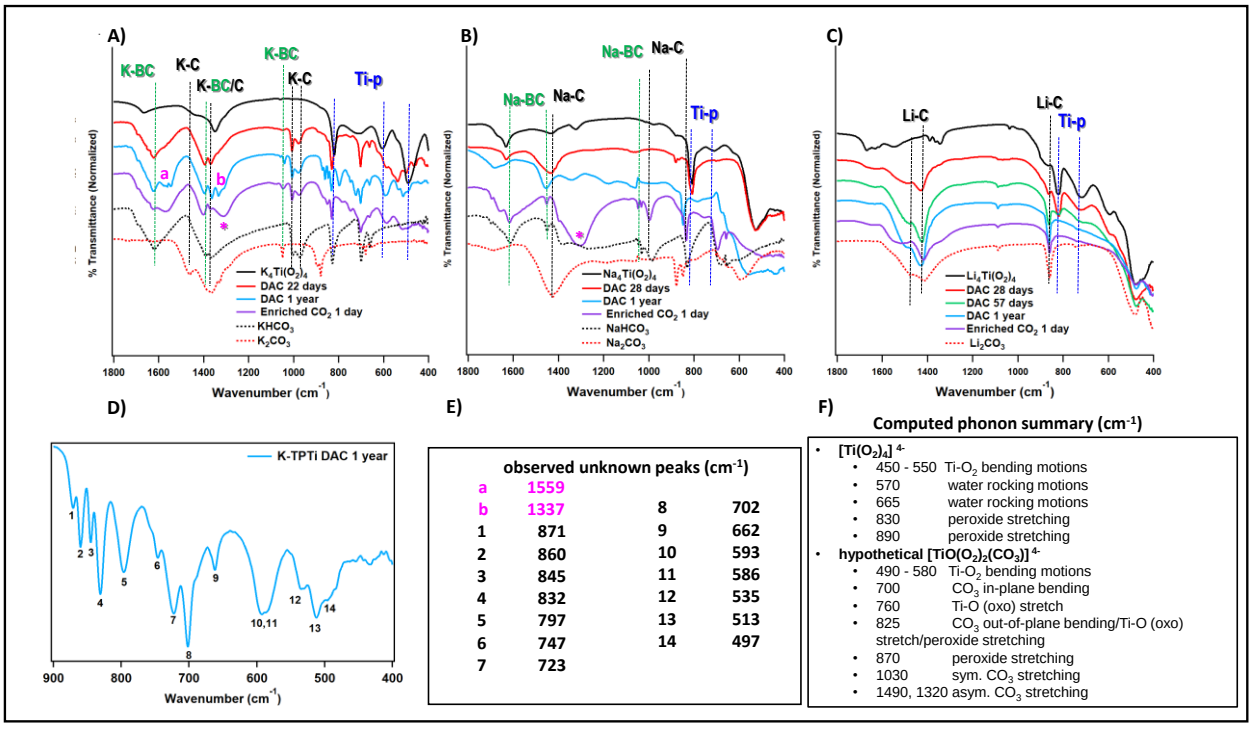

Figure 7. Summary of FTIR of DAC studies for K-**TPTi** (**A**), Na- **TPTi** (**B**), Li-**TPTi** (**C**). In parts A-C; Ti-p (blue) =titanium peroxide; A-BC (green) = alkali bicarbonate where A is Na or K; A-C (black) = alkali carbonate where A is Li, Na or K. Marked in pink 'a' and 'b' are unknown peaks, frequencies are listed in part **E**). **D)** Expanded spectrum (400-900 cm^{-1}) for K-**TPTi** 1-yr DAC products, and the numbered peaks are compiled in part **E**). **F**) Computed phonons for different vibrational modes for $Ti(O_2)_4^{4-}$ and hypothetical $TiO(O_2)_2(CO_3)^{4-}$ (illustrated in **figures S1.1 and S1.2**).

Na-**TPTi** FTIR spectra are more complex, due to the formation of both Na_2CO_3 (1428, 830 cm^{-1}) and $NaHCO_3$ (1611, 1454, 1033 cm^{-1}) as hydrolysis/autodegradation products, also in agreement with the TGA-MS. There are additionally peaks not identified as Ti-peroxide or carbonate/bicarbonate in the Na-**TPTi** from the CO_2-enriched environment, namely at 1306 cm^{-1}, also in the analogous K- **TPTi** sample (marked with a pink star). The K-**TPTi** (**figure 7A**), specifically at 1-yr DAC, exhibits much great complexity; including 1) splitting of the broad carbonate and bicarbonate peaks above 1300 cm^{-1}, and 2) additional peaks between 400 – 900 cm^{-1}. FTIR of the 1-yr DAC K-**TPTi** is shown in **figure 7D**, with the multiple unknown labeled peak positions listed in **figure 7E**. Without knowing the speciation of the DAC products, it is difficult to assign any of these peaks. However, based on the computational prediction that formation of hypothetical $TiO(O_2)_2(CO_3)^{4-}$ is even more favorable than the observed $VO(O_2)_2(CO_3)^{3-}$,[43] we have used this species as a model for partial description of DAC products and explanation of spectra of these unknown products. Listed in **figure 7F** is a summary of computed phonons for $Ti(O_2)_4^{4-}$ and hypothetical $TiO(O_2)_2(CO_3)^{4-}$ (vibrational modes illustrated in **figure S1B**). Multiple peaks for these titanium species are predicted from 450 – 1500 cm^{-1}. While this summary does not absolutely define the DAC products for K- **TPTi**, it affirms that the increased complexity in the vibrational spectra (compared to Li- **TPTi** and Na- **TPTi**) can be related to multiple bonding modes of Ti-oxo/carbonate/peroxide.

Raman of aqueous AOH/TiO_2/peroxide/CO_2 solutions

We attempted and did not succeed to crystallize Ti-carbonate-peroxide species from simple aqueous solutions, analogous to those from which the A-**TPTi** compounds were synthesized. However, aqueous phase Raman spectroscopy was a useful probe to study aqueous-phase bonding (**figure 8**). The solutions were prepared in the same way as the syntheses (**Table S1**), with the addition of infusing the solutions with CO_2 in the desiccator, similar to the solid phase CO_2-enriched atmosphere studies. The black spectrum in **figure 8** is aqueous $KHCO_3$, for which vibrational modes have been assigned,[65] to benchmark carbonate peak assignments. **Figure S5** and **S6** respectively show $A_4Ti(O_2)_4$ solid Raman spectra and $AHCO_3/A_2CO_3$ aqueous Raman spectra, in order to aid in assigning Ti-bound peroxide and Ti-bound carbonate. Although Davis[65] assigns the peak at 1283 cm^{-1} as COH bending, correlated with the 1030 cm^{-1} COH stretching peak, we note the broad bending peak is not present in the A_2CO_3 (aq) standards (A=Na, K, Cs). For this reason, we suggest the sharper 1030 cm^{-1} peak could alternatively be associated with a vibration mode of C-O. Based on comparison to the FTIR (**figure 4**) and Raman of $A_4Ti(O_2)_4$ crystals (**figure S5**), as well as computed vibrational modes (**figure S1.1**), we assign the broad double-peak between 810 cm^{-1} and 870 cm^{-1} as titanium-bound peroxide stretching motion that is observed in all three studied AOH/TiO_2/peroxide/CO_2 solutions. This is a similar frequency as that reported for uranyl-bound peroxide (840 cm^{-1})[30] and vanadium -bound peroxide (~870 cm^{-1})[42]. Both the solid-state Raman and FTIR exhibit a strong peak at ~500 cm^{-1}, which computation assigns as peroxide-Ti-peroxide bending motion (**figure S1.1a**). Interestingly, this peak is completely absent or significantly broadened in the solution Raman. This suggests the peroxide in these solutions is bound to larger, rigid species such as Ti-based polymers or

nanoparticles, likely induced by the decreased pH from CO_2 infusion, promoting olation/oxolation reactions.

The peak at 1358 cm^{-1} and shoulder at 1305 cm^{-1} are assigned as Ti-bound carbonate, based on comparison to Nb-bound carbonate,[66] which exhibits IR and Raman vibrations between 1200-1700 cm^{-1} that are attributed to metal-bound carbonate, with the benefit of a crystal structure. Also for comparison, Busca[67] attributes IR peaks at 1485 cm^{-1} and 1325 cm^{-1} to bidentate CO_3^{2-} on a TiO_2 surface. In addition, the carbonate stretches for azurite (copper carbonate) range between 1410 and 1460 cm^{-1}.[68] The peak observed at 1070 cm^{-1} is also attributed to Ti-associated carbonate. A similar peak is consistently observed in Nb-carbonate solutions and solids (1050 cm^{-1}). Finally, computation predicts Ti-bound carbonate stretch modes at numerous frequencies including 1025 – 1035 cm^{-1}, 1315 – 1345 cm^{-1}, and 1460 – 1500 cm^{-1} (**figure S1.2, figure 7F**). Based on this analysis, despite the inability to access crystal structures from these solutions, we believe these solutions present additional evidence for Ti-carbonate direct bonding, even in aqueous solution.

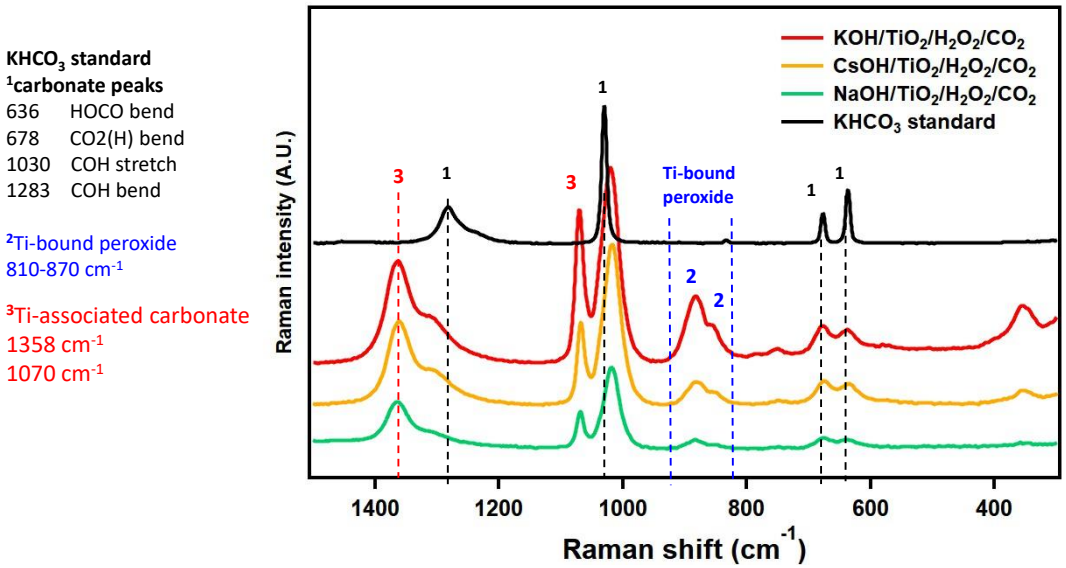

Figure 8. Raman spectra of aqueous AOH/TiO_2/peroxide/CO_2 solutions, evidencing Ti-carbonate bonding.

Scanning Electron Microscopy-Energy Dispersive X-ray Spectroscopy (SEM-EDX) of DAC products.

Finally, SEM imaging and elemental mapping of Na-T **TPTi** and K- **TPTi** (**figure 9**) provided additional evidence for the differentiating reaction pathways; by hydrolysis/autodegradation for Na-TPTi and Li- **TPTi** followed by DAC of the formed alkali-containing phases, and by Ti-centered DAC for K-**TPTi**. Since Li is below the atomic number limit for EDX detection, we could not provide the same analysis for Li- **TPTi** that we were able to obtain for Na- **TPTi** and K- **TPTi**. **Figure 9A** shows benched-aged Na-**TPTi** (30 days), looking down the 'cross section' of a large columnar-shaped crystal. There is an apparent core-shell type morphology. EDX analysis shows enrichment of Na in the shell, and Ti in the core. **Figure 9B** shows a different view of the core-shell morphology of degraded Na-**TPTi** (1 year ambient exposure), in addition to elemental mapping. The imaged degraded crystal resembles a hollow log, with the red star on the gray scale image and the Na/Ti colored map denoting the hollow core of the crystal (log). Elemental

mapping shows clear phase separation of Ti and Na. Specifically, EDX reveals 91/9 atomic % Ti/Na in the core, and the shell is the opposite; ~7/93% Ti/Na atomic % (**figure S7**). With the caveat that this is a semi-quantitative method, we can say that while there is definitely shell-enrichment of Na and core-enrichment of Ti, there is not complete separation, because the theoretical ratio of pristine A-TPTi is 80/20 atomic % A/Ti. At 30 days of ambient aging, the captured carbon of Na-TPTi remains quite low (**figure 5**), so the Na-rich surface of the degraded core-shell Na-TPTi crystals is clearly not as reactive towards DAC as K-TPTi (discussed below). TGA-MS discussed prior showed that abundant peroxide-bound Ti remains in Na-TPTi at 30 days ambient exposure, but based on **figures 9A and 9B** of these core-shell morphologies, access of the Ti-peroxide core is partially blocked by the Na-rich shell. This is additional indirect evidence that the titanium peroxide is the more effective DAC species than the sodium-rich passivating surface.

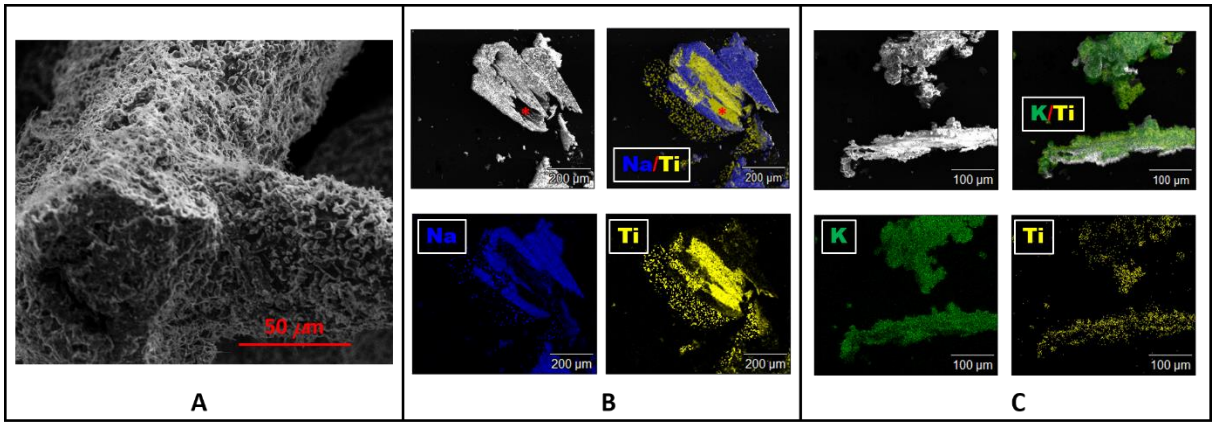

Figure 9. A) SEM gray-scale image of 30-day ambient exposed Na-**TPTi**, revealing the core-shell morphology. B) SEM gray-scale image plus elemental mapping of 1-year ambient exposed Na-**TPTi**, showing separation of Na and Ti rich phases. The red star highlights the center of the 'hollow log', indicating a core-shell morphology. C) SEM gray-scale image plus elemental mapping of 4-month ambient exposed K-**TPTi**, showing uniformity of K and Ti, without separation.

On the other hand, K-TPTi with four months of ambient exposure (**figure 9C**) exhibits a uniform distribution of K and Ti in the element map, and the composition of two surveyed areas is respectively 72/28 atomic % K/Ti, and 79/21 atomic % K/Ti (**figure S8**), where the latter represents ideal K-TPTi composition. Finally, the morphology of all the A-**TPTi** materials appear porous and spongy, particularly evident in the higher resolution images, **figure 9A** (Na-TPTi) and **figure S9** (K-TPTi). We presume this is related to the release of oxygen upon peroxide decomposition, whether by carbon capture or by hydrolysis/autodegradation (equations 1 - 3). The alkali surface passivation (observed definitively for Na-**TPTi**) that happens early during the aging studies may explain the delayed reactivity for Na-**TPTi** and Li-**TPTi**. Decomposition of peroxide in Ti-rich cores introducing porosity could allow the eventual CO_2 DAC of Na-**TPTi** and Li-**TPTi**, via access to the cores (for Na-**TPTi)**. PXRD tracked phase formation of all three A-TPTi materials as a function of ambient exposure (**figure S10**) for 35 days and 1 year, in addition to exposure to the CO_2-enriched environment. Consistent with the TGA-MS and the FTIR, these data showed the increasing presence of sodium/potassium carbonate and sodium/potassium bicarbonate for Na-**TPTi** and K-**TPTi**, and lithium carbonate for Li-**TPTi**. No anatase TiO_2 was detectable, based on the lack of the major peak at $2\theta = 25.3°$, shown as a standard in **figure S10**, and neither is rutile TiO_2 (not shown, $2\theta =$

27.1°). Therefore, any Ti-rich phases, including putative Ti-carbonate/peroxide phases as intermediates or products of DAC or hydrolysis/autodegradation, are amorphous.

Conclusions

In this study, we have presented a general synthetic approach to tetraperoxotitanates, their crystal structures, and their reactivity towards direct air capture of carbon dioxide. With these results, we now have three well-documented examples of the profound effect that the alkalis have on the reactivity of peroxometalates, the other two being $V^{V}(O_2)_4^{3-}$ and $U^{VI}O_2(O_2)_4^{4-}$. The studied $A_4Ti(O_2)_4$ (A=Li, Na, K) compounds exhibit differentiating reaction mechanism as a function of the alkali. The DAC mechanism of the K-analogue, with its rapid and high capacity (8.73 mmol CO_2/gram sorbent) reaction with atmospheric CO_2, can be best-described as a Ti-centered mechanism. On the other hand, the Li and Na analogues have delayed reactivity, due to autodegradation of the $Ti(O_2)_4^{4-}$ anion, separation of Ti-rich and alkali-rich phases, and passivation of the reactive titanium peroxide species (noted specifically for the Na-analogue). Future investigations include 1) Crystallization of Ti-carbonate and Ti-peroxide carbonate species to improve understanding of reaction mechanisms, and 2) Synthesis and DAC studies of alkaline earth peroxotitanates to better delineate the role of the counter cations, and ultimately optimize material performance metrics.

Acknowledgements. This work was supported by the Department of Energy under the grant DE-SC0022278. We acknowledge the Murdock Charitable Trust (grant SR-2017297) for acquisition of the SCXRD.

Supporting information available. Crystallographic information files (cif) can be obtained from the Cambridge Crystallographic Data Center (https://www.ccdc.cam.ac.uk/structures/) citing codes 2331364-2331366. Experimental methods and supplemental figures and data including crystallography, FTIR, Raman, computation, PXRD, SEM-EDX, and photos of lab setups and materials (PDF).

References

(1) Sanz-Pérez, E. S.; Murdock, C. R.; Didas, S. A.; Jones, C. W. Direct Capture of CO_2 from Ambient Air. *Chem Rev* **2016**, *116*, 11840-11876.

(2) Gao, W. L.; Liang, S. Y.; Wang, R. J.; Jiang, Q.; Zhang, Y.; Zheng, Q. W.; Xie, B. Q.; Toe, C. Y.; Zhu, X. C.; Wang, J. Y.; Huang, L.; Gao, Y. S.; Wang, Z.; Jo, C.; Wang, Q.; Wang, L. D.; Liu, Y. F.; Louis, B.; Scott, J.; Roger, A. C.; Amal, R.; Heh, H.; Park, S. E. Industrial carbon dioxide capture and utilization: state of the art and future challenges. *Chem Soc Rev* **2020**, *49*, 8584-8686.

(3) Panda, D.; Kulkarni, V.; Singh, S. K. Evaluation of amine-based solid adsorbents for direct air capture: a critical review. *React Chem Eng* **2022**, *8*, 10-40.

(4) Morrison, J.; Jauffret, G.; Galvez-Martos, J. L.; Glasser, F. P. Magnesium-based cements for CO_2 capture and utilisation. *Cement Concrete Res* **2016**, *85*, 183-191.

(5) Rausis, K.; Stubbs, A. R.; Power, I. M.; Paulo, C. Rates of atmospheric CO_2 capture using magnesium oxide powder. *Int J Greenh Gas Con* **2022**, *119*.

(6) de Jonge, M. M. J.; Daemen, J.; Loriaux, J. M.; Steinmann, Z. J. N.; Huijbregts, M. A. J. Life cycle carbon efficiency of Direct Air Capture systems with strong hydroxide sorbents. *Int J Greenh Gas Con* **2019**, *80*, 25-31.

(7) Zolfaghari, Z.; Aslani, A.; Zahedi, R.; Kazzazi, S. Simulation of carbon dioxide direct air capture plant using potassium hydroxide aqueous Solution: Energy optimization and CO_2 purity enhancement. *Energ Convers Man-X* **2024**, *21*.

(8) Grayevsky, R.; Reiss, A. G.; Emmanuel, S. Carbon Storage through Rapid Conversion of Forsterite into Solid Oxalate Phases. *Energ Fuel* **2023**, *37*, 509-517.

(9) Chouikhi, N.; Cecilia, J. A.; Vilarrasa-García, E.; Besghaier, S.; Chlendi, M.; Duro, F. I. F.; Castellon, E. R.; Bagane, M. CO_2 Adsorption of Materials Synthesized from Clay Minerals: A Review. *Minerals-Basel* **2019**, *9*.

(10) Reddy, M. K. R.; Xu, Z. P.; Lu, G. Q.; da Costa, J. C. D. Layered double hydroxides for CO_2 capture: Structure evolution and regeneration. *Ind Eng Chem Res* **2006**, *45*, 7504-7509.

(11) Zheng, S. X.; Song, C. H.; Curria, M. C.; Ren, Z. J.; White, C. E. Ca-Based Layered Double Hydroxides for Environmentally Sustainable Carbon Capture. *Environ Sci Technol* **2023**, *57*, 17212-17224.

(12) Veerabhadrappa, M. G.; Maroto-Valer, M. M.; Chen, Y. H.; Garcia, S. Layered Double Hydroxides-Based Mixed Metal Oxides: Development of Novel Structured Sorbents for CO_2 Capture Applications. *Acs Appl Mater Inter* **2021**, *13*, 11805-11813.

(13) Tao, Z. Y.; Tian, Y. M.; Ou, S. Y.; Gu, Q. F.; Shang, J. Direct air capture of CO_2 by metal cation-exchanged LTA zeolites: Effect of the charge-to-size ratio of cations. *Aiche J* **2023**, *69*.

(14) Rim, G.; Priyadarshini, P.; Song, M. Y.; Wang, Y. X.; Bai, A. D.; Realff, M. J.; Lively, R. P.; Jones, C. W. Support Pore Structure and Composition Strongly Influence the Direct Air Capture of CO_2 on Supported Amines. *J Am Chem Soc* **2023**, *145*, 7190-7204.

(15) Wu, Y. X.; Xu, J. H.; Mumford, K.; Stevens, G. W.; Fei, W. Y.; Wang, Y. D. Recent advances in carbon dioxide capture and utilization with amines and ionic liquids. *Green Chem Eng* **2020**, *1*, 16-32.

(16) Zheng, S.; Zeng, S. J.; Li, Y.; Bai, L.; Bai, Y. G.; Zhang, X. P.; Liang, X. D.; Zhang, S. J. State of the art of ionic liquid-modified adsorbents for CO_2 capture and separation. *Aiche J* **2022**, *68*.

(17) Ding, M. L.; Flaig, R. W.; Jiang, H. L.; Yaghi, O. M. Carbon capture and conversion using metal-organic frameworks and MOF-based materials. *Chem Soc Rev* **2019**, *48*, 2783-2828.

(18) Socolow, R.; Desmond, M.; Aines, R.; Blackstock, J.; Bolland, O.; Kaarsberg, T.; Lewis, N.; Mazzotti, M.; Pfeffer, A.; Sawyer, K.; Siirola, J.; Smit, B.; Wilcox, J. *Direct Air Capture of CO_2 with Chemicals, A Technology Assessment for the APS Panel on Public Affairs* for Society, A. P.2011.

(19) Knopf, I.; Ono, T.; Temprado, M.; Tofan, D.; Cummins, C. C. Uptake of one and two molecules of CO_2 by the molybdate dianion: a soluble, molecular oxide model system for carbon dioxide fixation. *Chem. Sci.* **2014**, *5*, 1772-1776.

(20) Silvia, J. S.; Cummins, C. C. Binding, release, and functionalization of CO_2 at a nucleophilic oxo anion complex of titanium. *Chemical Science* **2011**, *2*, 1474-1479.

(21) Grice, K. A. Carbon dioxide reduction with homogenous early transition metal complexes: Opportunities and challenges for developing CO_2 catalysis. *Coordin Chem Rev* **2017**, *336*, 78-95.

(22) Lawson, S.; Baamran, K.; Newport, K.; Rezaei, F.; Rownaghi, A. Screening of Adsorbent/Catalyst Composite Monoliths for Carbon Capture-Utilization and Ethylene Production. *Acs Appl Mater Inter* **2021**, *13*, 55198-55207.

(23) Ma, W.; Qiao, Y.; Theyssen, N.; Zhou, Q.; Li, D.; Ding, B.; Wang, D.; Hou, Z. A mononuclear tantalum catalyst with a peroxocarbonate ligand for olefin epoxidation in compressed CO_2. *Catal. Sci. Technol.* **2019**, *9*, 1621-1630.

(24) Phan, D. T.; Maeder, M.; Burns, R. C.; Puxty, G. Catalysis of CO_2 absorption in aqueous solution by vanadate and sulfate and their application to post combustion capture. *Int J Greenh Gas Con* **2015**, *36*, 60-65.

(25) Bhatti, U. H.; Shah, A. K.; Kim, J. N.; You, J. K.; Choi, S. H.; Lim, D. H.; Nam, S.; Park, Y. H.; Baek, I. H. Effects of Transition Metal Oxide Catalysts on MEA Solvent Regeneration for the Post-Combustion Carbon Capture Process. *Acs Sustain Chem Eng* **2017**, *5*, 5862-5868.

(26) Lai, Q. H.; Toan, S.; Assiri, M. A.; Cheng, H. G.; Russell, A. G.; Adidharma, H.; Radosz, M.; Fan, M. H. Catalyst-$TiO(OH)_2$ could drastically reduce the energy consumption of CO_2 capture. *Nat Commun* **2018**, *9*.

(27) Gao, H. X.; Huang, Y. F.; Zhang, X. W.; Bairq, Z. A. S.; Huang, Y. Q.; Tontiwachwuthikul, P.; Liang, Z. W. Catalytic performance and mechanism of SO_4^{2-}/ZrO_2/SBA-15 catalyst for CO_2 desorption in CO_2-loaded monoethanolamine solution. *Appl Energ* **2020**, *259*.

(28) Wood, P. C.; Ballou, E. V.; Spitze, L. A.; Wydeven, T. A Flow-System Comparison of the Reactivities of Calcium Superoxide and Potassium Superoxide with Carbon Dioxide and Water Vapor. *SAE Transactions* **1982**, *91*, 2932-2944.

(29) Kravchuk, D. V.; Dahlen, N. N.; Kruse, S. J.; Malliakas, C. D.; Shand, P. M.; Forbes, T. Z. Isolation and Reactivity of Uranyl Superoxide. *Angewandte Chemie-International Edition* **2021**, *60*, 15041-15048.

(30) Arteaga, A.; Arino, T.; Moore, G. C.; Bustos, J. L.; Horton, M. K.; Persson, K. A.; Li, J.; Stickle, W. F.; Kohlgruber, T. A.; Surbella, R. G.; Nyman, M. The Role of Alkalis in Orchestrating Uranyl-Peroxide Reactivity Leading to Direct Air Capture of Carbon Dioxide. *Chem Eur J* **2024**.

(31) Campbell, N. J.; Dengel, A. C.; Edwards, C. J.; Griffith, W. P. Studies on transition metal peroxo complexes. Part 8. The nature of peroxomolybdates and peroxotungstates in aqueous solution. *Dalton Trans.* **1989**, 1203-1208.

(32) Conte, V.; Floris, B. Vanadium and molybdenum peroxides: synthesis and catalytic activity in oxidation reactions. *Dalton Trans.* **2011**, *40*, 1419-1436.

(33) Grzywa, M.; Łasocha, W. Crystal structure of potassium and ammonium tetraperoxovanadates (V). *Z. Kristallogr. Cryst. Mater.* **2007**, *222*, 95-98.

(34) Grzywa, M.; Łasocha, W.; Rutkowska-Żbik, D. Structural investigation of tetraperoxo complexes of Mo (VI) and W (VI): X-ray and theoretical studies. *J. Solid State Chem.* **2009**, *182*, 973-982.

(35) Grzywa, M.; Nitek, W.; Łasocha, W. Synthesis, characterization and crystal structures of lithium tetraperoxomolybdate (VI) tetrahydrate $Li_2[Mo(O_2)_4]\cdot 4H_2O$ and lithium tetraperoxotungstate (VI) tetrahydrate $Li_2[W(O_2)_4]\cdot 4H_2O$. *J. Mol. Struct.* **2007**, *828*, 111-115.

(36) Grzywa, M.; Różycka, M.; Łasocha, W. Crystal structure of potassium tetraperoxomolybdate (VI) $K_2[Mo(O_2)_4]$. *Powder Diffr.* **2005**, *20*, 203-206.

(37) Haeuseler, H.; Wagener, M.; Müller, H. Preparation, Crystal Structure, and Vibrational Spectra of Rubidiumperoxoniobate (Rb_3NbO_8). *Z. Naturforsch. B* **1997**, *52*, 1082-1086.

(38) Schwendt, P.; Sivák, M.: Composition and Structure of Vanadium (V) Peroxo Complexes. ACS Publications, 1998.

(39) Schwendt, P.; Tatiersky, J.; Krivosudský, L.; Šimuneková, M. Peroxido complexes of vanadium. *Coord. Chem. Rev.* **2016**, *318*, 135-157.

(40) Wehrum, G.; Hoppe, R. On the constitution of peroxotantalates (V) with alkali metals: on the structure of $K_3Ta(O_2)_4$. *Z. Anorg .Allg. Chem.* **1993**, *619*.

(41) Won, T.-J.; Barnes, C. L.; Schlemper, E. O.; Thompson, R. C. Two crystal structures featuring the tetraperoxovanadate (V) anion and a brief reinvestigation of peroxovanadate equilibria in neutral and basic solutions. *Inorg. Chem.* **1995**, *34*, 4499-4503.

(42) Ribó, E. G.; Mao, Z. W.; Hirschi, J. S.; Linsday, T.; Bach, K.; Walter, E. D.; Simons, C. R.; Zuehlsdorff, T. J.; Nyman, M. Implementing vanadium peroxides as direct air carbon capture materials. *Chemical Science* **2024**, *15*, 1700-1713.

(43) Hirschi, J.; Nyman, M.; Zuehlsdorff, T. J. Electronic Structure and CO_2 Reactivity of Group IV/V/VI Tetraperoxometalates. *ChemRxiv, in review in J Phys Chem A* **2024**, *10.26434/chemrxiv-2024-blwjs*.

(44) Schwarz, V. R.; Giese, H. Uber die Peroxyde des Titans, Zirkons, Hafniums und Thoriums. *Zeitschrift für anorganische und allgemeine Chemie* **1928**, *176*, 209-232.

(45) Ghosh, J. K.; Jere, G. V. Solid-State Photodecomposition Studies of $K_4Ti(O_2)_4.2H_2O$,$K_3Ta(O_2)_2F_4$ and $K_2V2O_3(O_2)_2F_2$. *J Photoch Photobio A* **1987**, *40*, 295-306.

(46) Ghosh, J. K.; Jere, G. V. Solid-State Decomposition Study on Tetraperoxo Species of Transition-Metals .2. Kinetics of Isothermal Decomposition of $K_4[Ti(O_2)_4].2H_2O$. *Thermochim Acta* **1987**, *117*, 73-78.

(47) Muhlebach, J.; Muller, K.; Schwarzenbach, G. Peroxo Complexes of Titanium. *Inorg Chem* **1970**, *9*, 2381-+.

(48) Kondo, S.; Saruhashi, K.; Seki, K.; Matsubara, K.; Miyaji, K.; Kubo, T.; Matsumoto, K.; Katsuki, T. A μ-Oxo-μ-η^2:η^2-Peroxo Titanium Complex as a Reservoir of Active Species in Asymmetric Epoxidation Using Hydrogen Peroxide. *Angewandte Chemie-International Edition* **2008**, *47*, 10195-10198.

(49) Tang, S. D.; Deng, Y. F.; Fu, Z. Y. Synthesis, Crystal Structure and Pyrolysis of a Heterobimetallic Peroxo-titanium(IV) Nitrilotriacetate Complex. *Chinese J Struc Chem* **2010**, *29*, 1666-1671.

(50) Rohe, M.; Merz, K. Active peroxo titanium complexes: syntheses, characterization and their potential in the photooxidation of 2-propanol. *Chem Commun* **2008**, 862-864.

(51) Friese, D. H.; Hättig, C.; Rohe, M.; Merz, K.; Rittermeier, A.; Muhler, M. Oxidation of 2-Propanol by Peroxo Titanium Complexes: A Combined Experimental and Theoretical Study. *J Phys Chem C* **2010**, *114*, 19415-19418.

(52) Kholdeeva, O. A.; Maksimov, G. M.; Maksimovskaya, R. I.; Kovaleva, L. A.; Fedotov, M. A.; Grigoriev, V. A.; Hill, C. L. A dimeric titanium-containing polyoxometalate.: Synthesis, characterization, and catalysis of H_2O_2-based thioether oxidation. *Inorg Chem* **2000**, *39*, 3828-3837.

(53) Yaemsunthorn, K.; Tatarchuk, T.; Danyliuk, N.; Shyichuk, A.; Macyk, W. Yellow TiO_2 from titanium peroxo complexes: Verification of the visible light activity and a rational enhancement of its photocatalytic efficiency. *J Environ Chem Eng* **2023**, *11*.

(54) Sabale, S.; Bandgar, A.; Wang, H. Y.; Gurav, K.; Kim, J. H.; Pawar, S. H. Direct synthesis and characterization of high temperature stable anatase TiO_2 nanospheres from peroxo-titanium complex. *Met Mater Int* **2013**, *19*, 483-488.

(55) Yaminsky, I. V.; Akhmetova, A. I.; Kur'yakov, V. N.; Obolenskaya, L. N.; Kotlyarova, N. V. Hydrosols of Titanium Dioxide Nanoparticles Containing Ti(IV) Peroxo Complexes: Modification, Optical Properties, Morphology, and Bleaching Kinetics. *Inorg Mater+* **2020**, *56*, 1159-1166.

(56) Park, H.; Goto, T.; Cho, S. H.; Lee, S. W.; Kakihana, M.; Sekino, T. Effects of Annealing Temperature on the Crystal Structure, Morphology, and Optical Properties of Peroxo-Titanate Nanotubes Prepared by Peroxo-Titanium Complex Ion. *Nanomaterials-Basel* **2020**, *10*.

(57) Nyman, M.; Hobbs, D. T. A family of peroxo-titanate materials tailored for optimal strontium and actinide sorption. *Chemistry of Materials* **2006**, *18*, 6425-6435.

(58) Hossain, R.; Dickinson, J. J.; Apblett, A.; Materer, N. F. Detection of Hydrogen Peroxide in Liquid and Vapors Using Titanium(IV)-Based Test Strips and Low-Cost Hardware. *Sensors* **2022**, *22*.

(59) Hou, Y.; Fast, D. B.; Ruther, R. E.; Amador, J. M.; Fullmer, L. B.; Decker, S. R.; Zakharov, L. N.; Dolgos, M. R.; Nyman, M. The atomic level journey from aqueous polyoxometalate to metal oxide. *J Solid State Chem* **2015**, *221*, 418-425.

(60) Anderson, T. M.; Thoma, S. G.; Bonhomme, F.; Rodriguez, M. A.; Park, H.; Parise, J. B.; Alam, T. M.; Larentzos, J. P.; Nyman, M. Lithium polyniobates. A lindqvist-supported lithium-water adamantane cluster and conversion of hexaniobate to a discrete keggin complex. *Cryst Growth Des* **2007**, *7*, 719-723.

(61) Griffith, W. P.; Wickins, T. D. Studies on Transition-Metal Peroxy-Complexes .6. Vibrational Spectra and Structure. *J Chem Soc A* **1968**, 397-&.

(62) Paparo, A.; Silvia, J. S.; Spaniol, T. P.; Okuda, J.; Cummins, C. C. Countercation Effect on CO_2 Binding to Oxo Titanate with Bulky Anilide Ligands. *Chem-Eur J* **2018**, *24*, 17072-17079.

(63) Burlakov, V. V.; Dolgushin, F. M.; Yanovsky, A. I.; Struchkov, Y. T.; Shur, V. B.; Rosenthal, U.; Thewalt, U. Interaction of carbon dioxide with the bis(trimethylsilyl)acetylene complex of permethyltitanocene: Synthesis and structure of the binuclear carbonate complex of permethyltitanocene $(Cp_2*Ti)_2CO_3$. *J Organomet Chem* **1996**, *522*, 241-247.

(64) Duan, Y. H.; Zhang, B.; Sorescu, D. C.; Johnson, J. K.; Majzoub, E. H.; Luebke, D. R. Density functional theory studies on the electronic, structural, phonon dynamical and thermo-stability properties of bicarbonates $MHCO_3$, M = Li, Na, K. *J Phys-Condens Mat* **2012**, *24*.

(65) Davis, A. R.; Oliver, B. G. A Vibrational-Spectroscopic Study of the Species Present in the CO_2-H_2O System. *J Solution Chem* **1972**, *1*, 329-339.

(66) Mao, Z.; Rashwan, M.; Garrido-Ribo, E.; Nord, M.; Zakharov, L.; Surta, T. W.; Uysal, A.; Nyman, M. Carbon Dioxide Capture by Niobium Polyoxometalate Fragments. *ChemRxiv, in review in JACS* **2024**, *10.26434/chemrxiv-2024-nxrfz*.

(67) Busca, G.; Lorenzelli, V. Infrared Spectroscopic Identification of Species Arising from Reactive Adsorption of Carbon Oxides on Metal-Oxide Surfaces. *Mater Chem* **1982**, *7*, 89-126.

(68) Alves, J. F.; Edwards, H. G. M.; Korsakov, A.; de Oliveira, L. F. C. Revisiting the Raman Spectra of Carbonate Minerals. *Minerals-Basel* **2023**, *13*.

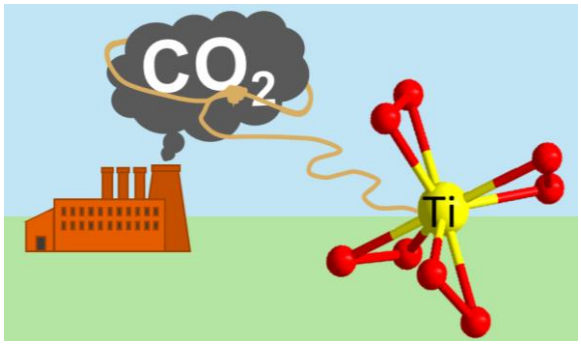

For Table of Contents Only